



## Article

# Estimation of Vertical Phase Center Offset and Phase Center Variations for BDS-3 B1CB2a Signals

Shichao Xie <sup>1</sup>, Guanwen Huang <sup>1,2,\*</sup>, Le Wang <sup>1</sup>, Xingyuan Yan <sup>3,4</sup> and Zhiwei Qin <sup>1</sup> <sup>1</sup> College of Geology Engineering and Geomatics, Chang'an University, Xi'an 710054, China<sup>2</sup> Key Laboratory of Ecological Geology and Disaster Prevention, Ministry of Natural Resources, Xi'an 710054, China<sup>3</sup> School of Geospatial Engineering and Science, Sun Yat-sen University, Zhuhai 519000, China<sup>4</sup> Key Laboratory of Natural Resources Monitoring in Tropical and Subtropical Area of South China, Ministry of Natural Resources, Guangzhou 510600, China

\* Correspondence: guanwen@chd.edu.cn; Tel.: +86-136-3680-1167

**Abstract:** The BeiDou Global Satellite Navigation System (BDS-3) broadcast newly developed B1C and B2a signals. To provide a better service for global users, the vertical phase center offset (PCO) and phase center variation (PCV) are estimated for the B1C/B2a ionospheric-free linear combination of the BDS-3 inclined geostationary orbit (IGSO) and medium earth orbit (MEO) satellites in this study. And considering the traditional PCC estimation method needs two Precise orbit determination (POD) processing, based on the correlation between PCO z-offset and PCV, the theoretical analysis and experimental comparison have been made to discuss whether the POD procedure for the PCO estimation can be omitted. The estimated z-offset time series revealed the inadequacy of the solar radiation pressure (SRP) model for the IGSO satellites and the MEO satellites with Pseudo Random Noise code (PRN) C45 and C46. The PCVraws estimated by the traditional method and the PCO estimation omitted method have the same characteristic. The final PCO z-offsets and PCVs calculated by the two schemes agreed very well with differences can be harmlessly ignored, which confirmed that the PCO estimation can be safely omitted to save computation time. The PCC model proposed in this study has been compared with the Test and Assessment Research Center of China Satellite Navigation Office (TARC/CSNO) released model, the qualities of the orbits and BDS-only precise point positioning (PPP) solutions of the new model both show improvements, except for the IGSO orbits. The analysis of the IGSO orbits further verifies the SRP model is not suitable for the IGSO satellites.

**Keywords:** BDS-3; B1CB2a; phase center correction models; precise orbit determination; IGb14

**Citation:** Xie, S.; Huang, G.; Wang, L.; Yan, X.; Qin, Z. Estimation of Vertical Phase Center Offset and Phase Center Variations for BDS-3 B1CB2a Signals. *Remote Sens.* **2022**, *14*, 6380. <https://doi.org/10.3390/rs14246380>

Academic Editors: Baocheng Zhang and Teng Liu

Received: 8 November 2022

Accepted: 15 December 2022

Published: 16 December 2022

**Publisher's Note:** MDPI stays neutral with regard to jurisdictional claims in published maps and institutional affiliations.



**Copyright:** © 2022 by the authors. Licensee MDPI, Basel, Switzerland. This article is an open access article distributed under the terms and conditions of the Creative Commons Attribution (CC BY) license (<https://creativecommons.org/licenses/by/4.0/>).

## 1. Introduction

On 31 July 2020, the construction of the BeiDou Global Satellite Navigation System (BDS-3) has been officially announced completeness and BDS-3 started to provide positioning, navigation, and timing (PNT) service globally with 3 geosynchronous orbit (GEO) satellites, 3 inclined geostationary orbit (IGSO) satellites, and 24 medium earth orbit (MEO) satellites in-orbit [1]. Different from the BeiDou Regional Satellite Navigation System (BDS-2), in addition to signals at frequencies B1I (1561.098 MHz) and B3I (1268.52 MHz), BDS-3 also transmit the newly designed signals at frequencies B1C (1575.42 MHz), B2a (1176.45 MHz), and B2b (1207.14 MHz) [2]. B1C/B2a can be chosen for dual-frequency usage [3], the B1C and B2a signals are designed to be compatible with GPS L1C, Galileo E1 and GPS L5, Galileo E5 open service signals, respectively [4,5], therefore the B1C/B2a signals are more compatible and interoperable with other Global Navigation Satellite System (GNSS). The multi-GNSS applications require all navigation system products in the same reference frame, this requests the consistency of the phase center correction (PCC) model, which is comprised of phase center offset (PCO) and phase center variation (PCV) [6]. Due

to the lack of observations for B1C/B2a signals, current precise products and studies of PCC models for BDS-3 are mainly based on B1I/B3I signals. To improve the multi-GNSS application service performance of BDS-3, this study focuses on the B1C/B2a signals.

The current studies of B1C/B2a signals mainly focus on performance evaluation. Zhang et al. [7] evaluated the characteristics of the B1C, B1I, B2a, B2b, and B3I signals and the result revealed that the quality of the BDS-3 signals is equivalent to that of GPS L1/L2/L5 and Galileo E1/E5a/E5b signals. The study of Yan et al. [8] indicated that B1C has a lower C/N0, and the C/N0 of B2a and B1I/B3I signals are at the same level. Zhang et al. [9] reported that the observation noise of the new B1C and B2a signals is smaller than B1I, and the Single Point Positioning (SPP) performance of B1C is similar to that of B1I, but that of B2a is slightly worse, which may cause by inaccurate BDS ionosphere correction. Li et al. [5] analyzed the Precise orbit determination (POD) capacity of B1C/B2a signals using only nine of the Multi-GNSS Experiment (MGEX) stations, the result shows that the 3D RMS values of the two-day overlap of the orbit determined using B1C/B2a are improved by approximately 9% compared to that of the orbit determined using B1I/B3I across the whole BDS-3 constellation. In general, the study and usage of B1C/B2a signals are insufficient, the relevant models need to pay more attention, especially the PCC models.

The International GNSS Service (IGS) published the igs14.atx to be consistent with the IGB14 frame, the igs14.atx contains the PCC models of GNSS satellites and receiver antennas, for GPS and GLONASS, the PCC models are based on the in-orbit estimation results of different Analysis Centers (AC) [10]; different from GPS and GLONASS, the PCC models of Galileo were calibrated pre-launch and released by the European GNSS Agency (GSA). The satellite-specific PCOs for BDS satellites have been released by The Test and Assessment Research Center of China Satellite Navigation Office (TARC/CSNO) [11] and adopted by IGS to conduct satellite-block-specific BDS-3 PCOs for igs14.atx (IGS Mail 7782). Several efforts have been made for BDS PCC model refinements. Dilssner et al. [12], Guo et al. [13], and Huang et al. [14] have estimated the BDS-2 PCC models to keep consistency with the IGB08 framework; Yan et al. [15], Xia et al. [16] (2020), Qu et al. [17], and Zajdel et al. [18] have studied the BDS-3 PCC models in IGB14 framework, but all the works are done for B1I/B3I signals, except for the work of Zajdel et al. [18], they evaluated the usage of the BDS-3 MEO constellation to the definition of the TRF scale and estimated the PCO models for both B1I/B3I and B1C/B2a signals. No comprehensive PCVs were available for BDS-3 B1C/B2a signals until now.

PCO is a vector pointing from the center of mass (COM) to the antenna phase center (APC) in a satellite body-fixed coordinate system, which can be defined by x-offset, y-offset, and z-offset [19], the x-offset and y-offset form the horizontal PCO, and z-offset is vertical PCO. The horizontal PCO only has a negligible impact on the scale realization [18]; and as reported by the previous study, there is a high correlation coefficient between the horizontal PCO and the solar radiation pressure (SRP) parameters [20], therefore, the study of horizontal PCO is not within the scope of this study. The vertical PCO is critical for GNSS data processing, especially on scale realization, as the z-offset is always direct to the center of the earth [21,22]. The PCV and z-offset also have strong correlations; generally, the PCV and PCO are estimated separately; first, the PCO is estimated with PCV fixed, then fix the PCO to estimate the PCVraw, and finally, the correction of z-offset and PCV are derived from PCVraw [6,22,23]. Since the PCO and PCVraw are estimated by a POD process, the whole data processing procedure above mentioned is quite time-consuming, and a concise way to get vertical PCO and PCV needs to be discussed.

This study aims to estimate the vertical PCO and PCV models for BDS-3 IGSO and MEO satellites B1C/B2a ionospheric-free linear combination with CSNO published PCO models as initial models, and a time-saving 2-Step Scheme by only estimating PCVraw to get vertical PCO and PCV is discussed and validated. Section 2 discussed the PCC model with a focus on the PCVraw model and estimation method used in this study. Section 3 introduced the data availability and basic models of data processing. The estimated z-offset and PCV are discussed in Section 4. The quality of the proposed final PCO z-offset and

PCV are verified by orbit and BDS-only precise point positioning (PPP) quality in Section 5. Finally, Section 6 gives a summary and discussion of this study.

## 2. PCC Model

### 2.1. Basic Model

The PCO correction in GNSS data processing is expressed as a vector correction:

$$\vec{r}' = \vec{r} + \begin{pmatrix} \vec{e}_x & \vec{e}_y & \vec{e}_z \end{pmatrix} \begin{bmatrix} \Delta x_{PCO} \\ \Delta y_{PCO} \\ \Delta z_{PCO} \end{bmatrix} = \vec{r} + \mathbf{R} \cdot \vec{P} \tag{1}$$

where  $\vec{r}'$  is a vector pointing to satellite APC by receiver APC,  $\vec{r}$  is a vector pointing to satellite COM by receiver APC.  $\vec{e}_x$ ,  $\vec{e}_y$ , and  $\vec{e}_z$  are the unit vector of the +X-axis, +Y-axis, and +Z-axis of the satellite body-fixed reference frame in the Geocentric Celestial Reference System (GCRS), respectively.  $\Delta x_{PCO}$ ,  $\Delta y_{PCO}$ , and  $\Delta z_{PCO}$  are the PCO x-offset, PCO y-offset, and PCO z-offset, respectively.  $\vec{P}$  denotes the PCO vector, which consists of  $\Delta x_{PCO}$ ,  $\Delta y_{PCO}$ , and  $\Delta z_{PCO}$ .  $\mathbf{R}$  means the rotation matrix, which consists of  $\vec{e}_x$ ,  $\vec{e}_y$ , and  $\vec{e}_z$  [14]. The estimated PCO model is based on Equation (1) and converted to a distance correction ( $\Delta\rho$ ), since only z-offset is studied in this paper, the correction can be:

$$\Delta\rho(\eta) = \Delta z_{PCO} \cos \eta \tag{2}$$

$\eta$  is the nadir angle, which is seen from the satellite to the station.

The PCVraw is modeled as a piece-wise linear model Equation (3). The PCVraw is estimated together with the satellite clock offset that does not depend on the nadir-angle, these two parameters have a strong correlation, therefore, to avoid the normal equation being singular, a priori constraint Equation (4) is applied for the PCVraw estimation [23]:

$$\Delta\rho'_{PCV}(\eta) = \frac{\eta - \eta_j}{\eta_{j+1} - \eta_j} (\Delta\rho'_{PCV}(\eta_{j+1}) - \Delta\rho'_{PCV}(\eta_j)) + \Delta\rho'_{PCV}(\eta_j) \tag{3}$$

$$\sum_{i=1}^n \Delta\rho'_{PCV}(\eta_i) = 0 \tag{4}$$

$\Delta\rho'_{PCV}(\eta)$  is the satellite PCVraw value at the nadir-angle ( $\eta$ ).  $n$  is the node number of the piece-wise linear model. The subscript  $j$  in Equation (3) denotes the nearest integer nadir-angle less than  $\eta$ , and the subscript  $i$  in Equation (4) is the marker of one integer nadir-angle. The estimated satellite PCVraw consisted of satellite PCV ( $\Delta\rho_{PCV}$ ) and the PCO z-offset correction ( $\Delta z$ ), which can be expressed as follows [23]:

$$\Delta\rho'_{PCV}(\eta) = \Delta\rho_{PCV}(\eta) + \Delta z(1 - \cos \eta) \tag{5}$$

Figure 1 is a brief demonstration of the geometric relation of the estimated PCC model parameters. It is very clear that the estimated PCVraw, i.e.,  $\Delta\rho'_{PCV}$ , consists of the PCV ( $\Delta\rho_{PCV}$ ) and the PCO z-offset correction ( $\Delta z$ ), their relationship is described as Equation (5).

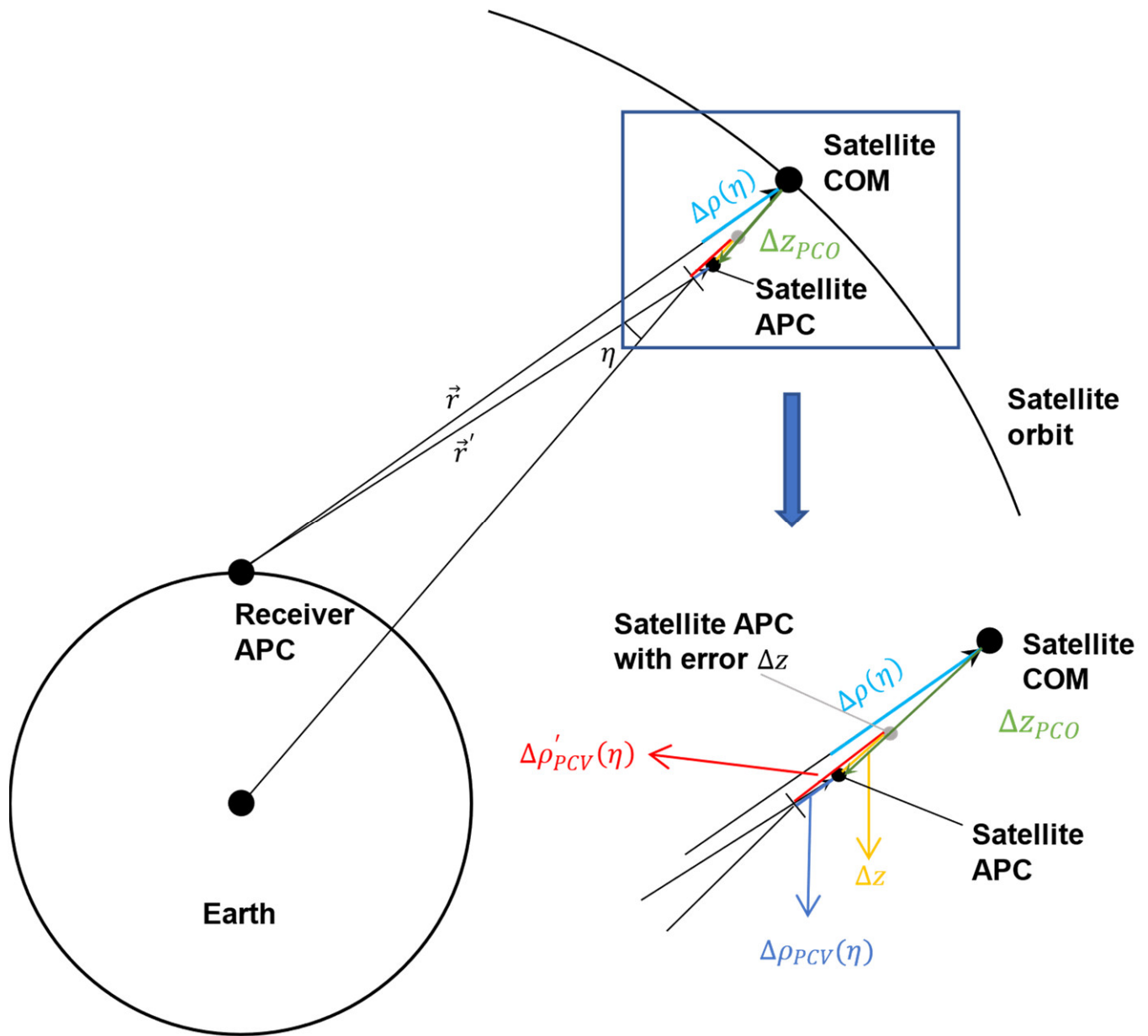


Figure 1. The geometric relation of the estimated PCC model parameters.

### 2.2. Estimation Methods

The PCO and PCV are estimated by a POD process, and the basic observations are the pseudo-range and carrier-phase observations. The BDS-3 B1C/B2a and GPS L1/L2 dual frequencies observations are used to form ionospheric-free linear combinations to eliminate the first-order ionospheric delay. The ionospheric-free pseudo-range observation can be described as follows:

$$P_{IF} = \left| \vec{r}' \right| + c(\tau_k - \tau^s) + \Delta\rho_{tro} - \Delta\rho_{PCV} + \Delta\rho_{k,PCV} + \varepsilon_P \quad (6)$$

where  $P_{IF}$  is the ionospheric-free pseudo-range observation;  $\left| \vec{r}' \right|$  denotes the distance from the satellite APC to receiver APC;  $c$  is the speed of light;  $\tau_k$  and  $\tau^s$  are the receiver clock offset and satellite clock offset, respectively,  $\Delta\rho_{tro}$  is the tropospheric delay;  $\Delta\rho_{k,PCV}$  is the receiver PCV correction;  $\varepsilon_P$  is the other ionospheric-free pseudo-range range error

including the observation noise. The ionospheric-free carrier-phase observation can be described as follows:

$$L_{IF} = \left| \vec{r}' \right| + c(\tau_k - \tau^s) + \Delta\rho_{tro} - \Delta\rho_{PCV} + \Delta\rho_{k,PCV} + \lambda N + \varepsilon_L \quad (7)$$

where  $L_{IF}$  is the ionospheric-free carrier-phase observation;  $\lambda$  is the wave length;  $N$  denotes the ionospheric-free ambiguity;  $\varepsilon_L$  is the other ionospheric-free carrier-phase range error, including the observation noise.

As mentioned in Section 1, the PCC estimation usually needs three steps. Firstly, the PCO is estimated with PCV fixed, since no officially published or widely recognized PCV is available for BDS-3 B1C/B2a signals, the PCV usually fix to zero, consequently, errors will be introduced to the estimated z-offset; secondly, with estimated PCO fixed, PCVraw are estimated; finally, the z-offset correction and PCV can be separated from PCVraw by a least square adjustment built according to Equation (5) with the following criterion [24]:

$$\sum_{i=1}^n [\Delta\rho'_{PCV}(\eta_i) - a - \Delta z(1 - \cos \eta_i)]^2 = \min \quad (8)$$

$a$  is the constant part of  $\Delta\rho'_{PCV}(\eta_i)$ . This estimation method needs 2 POD processes for PCO and PCVraw estimation, respectively. The PCO estimation process can provide a precise initial value of z-offset for the PCVraw estimation, and the  $\Delta z$  separated from PCVraw is mainly introduced by the unmodeled PCV used in PCO estimation.

From Equation (5) and Figure 1, we can see that the PCVraw can absorb the error that exists in the PCO z-offset. If the PCO estimation process is omitted, all errors that exist in the initial PCO z-offset will be introduced to the PCVraw. As PCVraw and the least square adjustment have been well modeled, a coarse initial PCO z-offset can be fixed for PCVraw estimation, and the error of this PCO z-offset can be well absorbed by PCVraw and derived to  $\Delta z$ , hence, the POD process for PCO estimation can be omitted to reduce the data processing time and burden. Above all, a 2-Step Scheme that omits the PCO estimation step for the PCO z-offset and PCV estimation is proposed, the detailed process procedures are the follows:

*Step 1:* Fix the PCO z-offset to a coarse initial value, estimate the daily PCVraw by POD process, and derive the satellite-specific PCVraw;

*Step 2:* Use the least square adjustment established based on Equation (8) to derive the satellite-specific PCV and PCO z-offset corrections from the satellite-specific PCVraw to get the final PCO z-offset and PCV.

The main difference between the proposed 2-Step Scheme and the traditional 3-Step Scheme is the way they handle the error of the initial PCO z-offset. In the 3-Step Scheme, the PCO estimation step corrects the main part of the error of the initial PCO z-offset, while in the 2-Step Scheme, the whole error is absorbed to the PCVraw, and the final least square adjustment can split the PCVraw to PCV and PCO z-offset correction, i.e.,  $\Delta z$ , precisely. To verify the proposed method, we have estimated 2 sets of PCO z-offset and PCV using the traditional 3-Step Scheme and the 2-Step Scheme, which omit the PCO estimation, the results and comparisons are discussed in Section 4.

### 3. Processing Strategy

#### 3.1. Data Availability

The major restriction of B1C/B2a precise data processing is the lack of tracking stations. Thankfully, with the development of MGEX, the number of MGEX with the capability of tracking B1C/B2a signals has grown rapidly in recent years, mainly attribute to firmware and hardware updates. A network of 120 globally distributed MGEX tracking stations has been selected for the data processing, as shown in Figure 2. The data collection time period is from Day of Year (DOY) 180, 2021, to DOY 179, 2022.

Figure 3 shows the daily number of stations used in B1C/B2a data processing for the selected BDS satellites (C20, C37, C40, C46) across the time period, G12 (L1/L2) is selected as a reference. The daily station number of C20 and C37 is nearly the same and the most among all selected BDS-3 satellites, as they are one of the 18 MEO satellites of the BDS-3 basic system, the basic system has been announced to begin providing initial services to global users on December 27, 2018 [25]. The daily station number of C40 is the least because C40 is an IGSO satellite, and its signal covers only the Asia-pacific area. The daily station number of all selected BDS-3 satellites are increase over time and reaches the level of GPS at the end of the chosen time period except C40.

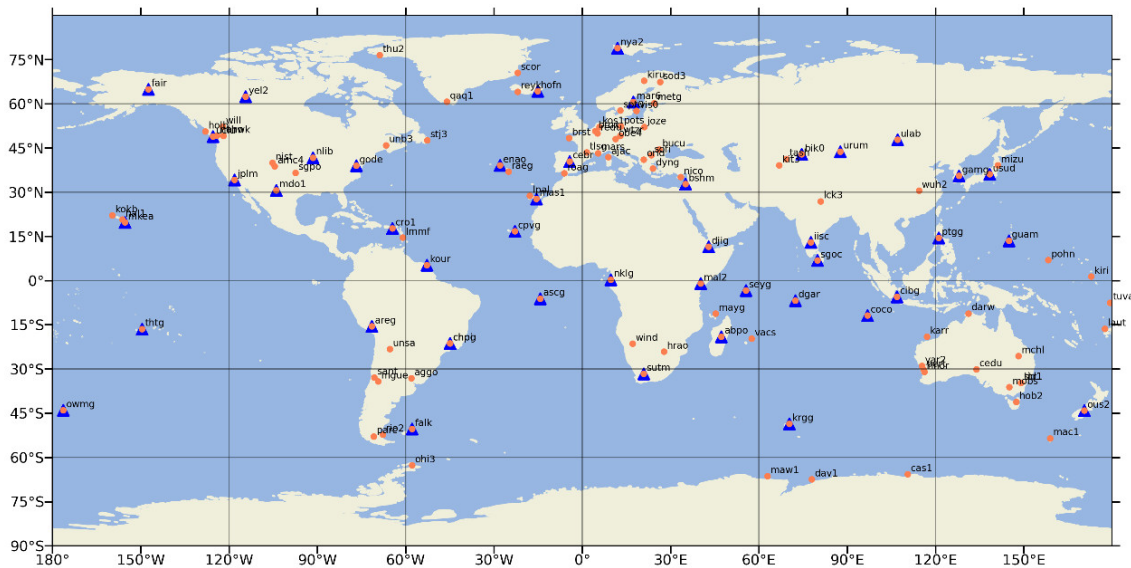


Figure 2. Distribution of the tracking stations, coral dots denote the stations used for POD, and blue triangles denote stations used for the BDS-only PPP in validations.

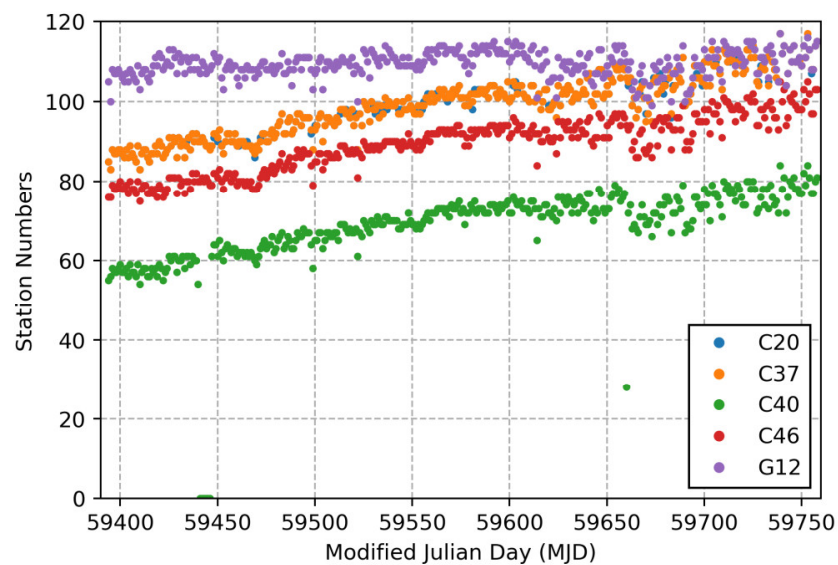


Figure 3. Daily number of stations used for the data processing of the selected BDS satellites (C20, C37, C40, C46) and GPS satellite G12, the signal frequencies pair are B1C/B2a for BDS and L1/L2 for GPS.

### 3.2. Basic POD Models and Strategies

The PCO z-offset, zenith path delays (ZPDs), and station heights have strong correlations and a huge impact on the reference frame realization [18,21,22]. To estimate z-offset and PCV, the framework must be fixed [24]. The GPS PCC model and the IGS weekly solutions of MGEX station coordinates are strictly realizations of the IGS14 scale, hence they are fixed in the data processing, BDS-3 and GPS are processed together as well. The receiver antennas PCC models also play an important role in framework realization, the IGS14.atx provides all receiver antennas PCC models for GPS L1/L2 signals, unfortunately, only a few antenna PCC models for BDS B1C/B2a signals are provided in IGS14.atx [24]. In the IGS third reprocess, some antennas PCC models for BDS signals have been calibrated by Geo++ and released in the igsR3\_2077.atx, these antennas cover more than 160 MGEX stations [17], for these stations the receiver antennas PCC models in igsR3\_2077.atx are used for BDS B1C/B2a signals, and for the other stations, PCC models for GPS L1/L2 signals were used instead [24].

The modeling of the non-gravitational perturbing forces is essential for POD. Solar radiation pressure (SRP) is the main non-gravitational force acting on GNSS satellites [26]. The reduced empirical CODE (Center for Orbit Determination in Europe) orbit model (ECOM1) [27,28] has been proven to be efficient for GPS POD, but for BDS-3 satellites with an elongated body, the ECOM2 [29] or ECOM1 with a priori box-wing model is more suitable. Li et al. [30] proved that the BDS-3 orbit satellite laser ranging (SLR) residuals with the ECOM2 SRP model are more scattered than that of ECOM1 with a priori box-wing model, hence, the latter is used for BDS-3 data processing, and the satellite metadata a priori box-wing model required is released by CSNO [31], these metadata also used for the ERP model. The Earth radiation pressure (ERP) and Antenna thrust (AT) are other main sources of non-gravitational force, they will cause a nearly 30 mm bias in total in the radial direction for BDS-3 satellites [32]. The ERP and AT are corrected by a model developed by Rodriguez-Solano [33], and the antenna transmitting power used in the model is published by IGS [34,35]. Table 1 is the overall data processing strategies.

**Table 1.** Data processing strategies.

Items	Description
Number of stations	≈120 MGEX stations
Time interval	DOY 180, 2021 to DOY 179, 2022
Observation	Zero-difference phase and code observation for GPS L1/L2 and BDS-3 B1C/B2a dual-frequency signals
Sampling rate	300 s
Elevation cut-off angle	7°
Arc length	24-h
Ionosphere	Ionosphere-free linear combination
Troposphere	Saastamoinen model [36] used as a priori model; ZTDs at 2 h interval is estimated; horizontal gradients estimated at 6 h interval with Global Mapping Function (GMF) [37]
Ambiguity fixing	Double-difference ambiguity fix [38]
Stations coordinates	Fixed
Solar radiation model	GPS: ECOM1 BDS-3: ECOM1 + a priori box-wing model
Earth radiation model	Box-wing [33]
Antenna thrust	GPS: 50–300 W [34] BDS-3: 130–310 W [34,35]
Satellites PCOs	GPS: igs14_2223.atx BDS-3: CSNO published model as a priori model
Satellites PCVs	GPS: igs14_2223.atx BDS-3: Zero as initial value
Receiver PCC	GPS: igs14_2223.atx BDS-3: igsR3_2077.atx or using L1/L2 for B1C/B2a

#### 4. Results of PCO-Z and PCVs

As mentioned in Section 2.2, the vertical PCO and PCV are estimated by two schemes: the traditional 3-Step Scheme and the 2-Step Scheme with PCO estimation omitted. The z-offsets estimated in the 3-Step Scheme are described in Section 4.1 and the PCVraw estimation and separation of both schemes are described and compared in Section 4.2.

##### 4.1. PCO-Z Parameters of the 3-Step Scheme

The estimated PCO z-offset is the correction of the initial PCO z-offset, in this study, the initial PCO z-offset is the CSNO-published value. The BDS-3 satellites are provided by two manufacturers: the Shanghai Engineering Center for Microsatellites (SECM) and the China Academy of Space Technology (CAST). The SECM provides 10 MEO satellites, and the CAST provides the other 14 MEO satellites and 3 IGSO satellites. The z-offsets time series of C23 (SVN C209), C29 (SVN C207), and C40 (SVN C224) are selected and shown in Figure 4 as representative of CAST MEO, SECM MEO, and IGSO satellites, respectively, the z-offsets time series of C46 (SVN C223) is also shown as a representative of C45 (C222) and C46 because of their different behaviors.

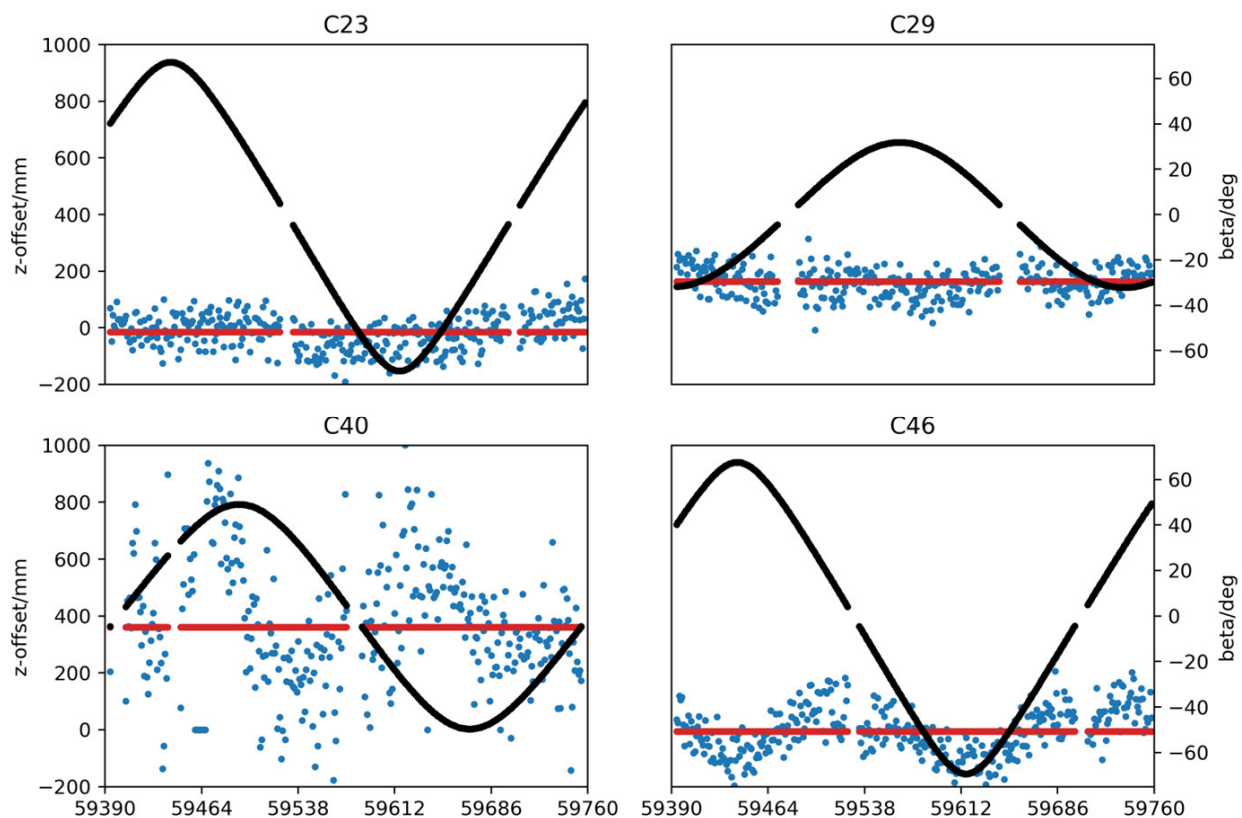


**Figure 4.** The z-offset time series of C23, C29, C40, and C46, respectively. The blue dots are z-offsets, the black dots are the beta angles, and the red dots are the derived z-offsets.

Figure 4 demonstrates that the z-offset time series of C23 and C29 are stable, the series of C40 is more scattered and varies with the sun elevation above the orbital plane ( $\beta$  angle), and the series of C46 shows a clearer variation with the  $\beta$  angle. The BDS-3 IGSO satellites are not standard Box-Wing structure, they carry additional payloads like communication antennas (Figure 5), and these payloads are not considered in the Box-Wing nor the ECOM SRP modeling, the additional payloads caused deficiencies to the IGSO SRP model and therefore introduce errors to the IGSO orbits and z-offset estimations. The C45/C46 PCO estimations of Zajdel et al. [18] show the same behaviors as Figure 4, according to Zajdel et al., these satellites may have different structures, which results in

the SRP model deficiency and affect the z-offset estimations. The satellite-specific z-offsets are acquired by taking the average of estimations at  $|\beta| > 4^\circ$  and are shown as red dots in Figure 4. The estimations at  $|\beta| \leq 4^\circ$  are excluded because the satellites may be in eclipse season during  $|\beta| \leq 4^\circ$ . In the eclipse season, the satellites suffer more complex space environments than usual, which will cause the estimated z-offsets to be more scattered. Therefore, the estimations at  $|\beta| \leq 4^\circ$  may contaminate the final results. Table 2 list the estimated z-offsets (z-offset), the RMSEs of estimated z-offsets (RMSE), and the final satellite-specific PCO z-offset (PCO-Z). The RMSEs of C45, C46, and IGSO satellites are larger than that of the others. Figure 6 shows the relationship of the initial PCO-Z, the estimated z-offsets (z-offset), and the final PCO-Z (PCO-Z in Table 2).

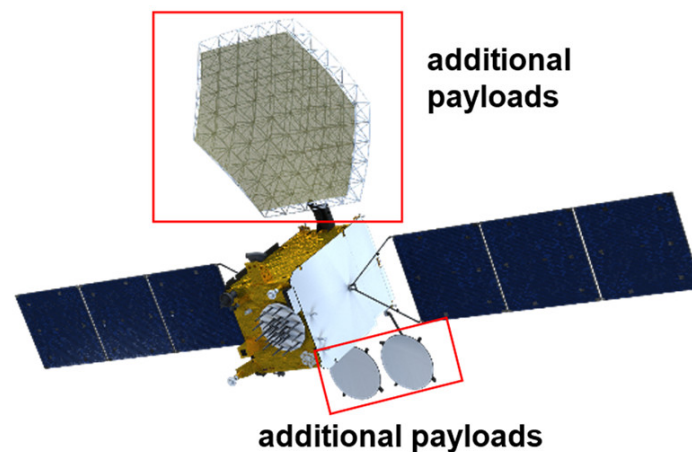


**Figure 5.** The structure of BDS-3 IGSO satellites (<http://www.csno-tarc.cn/en/system/introduction> (accessed on 7 November 2022)).

**Table 2.** Final satellite-specific PCO z-offset, the unit is mm.

PRN	z-Offset	RMSE	PCO-Z	PRN	z-Offset	RMSE	PCO-Z
C19	−99.24	69.69	1880.48	C34	−34.94	57.18	1073.17
C20	−110.30	65.01	1935.26	C35	−100.47	57.46	997.82
C21	−108.91	69.06	1898.07	C36	−33.91	59.59	1782.81
C22	−111.87	71.19	1910.18	C37	−62.96	57.42	1792.05
C23	−14.92	60.02	1950.06	C38	199.21	158.68	2744.77
C24	−13.08	66.54	1999.41	C39	304.75	213.11	2810.12
C25	−65.01	63.31	1038.91	C40	361.33	228.24	2877.62
C26	−39.24	82.28	1068.55	C41	277.91	72.86	1823.20
C27	110.54	45.05	1225.97	C42	288.23	63.17	1832.81
C28	105.66	52.72	1218.22	C43	5.00	73.70	1110.45
C29	164.27	50.81	1284.07	C44	−90.66	68.96	1011.32
C30	154.95	68.52	1249.08	C45	−16.33	94.91	1862.69
C32	−33.27	66.74	1961.20	C46	−5.09	85.66	1856.54
C33	39.50	67.84	1989.29				

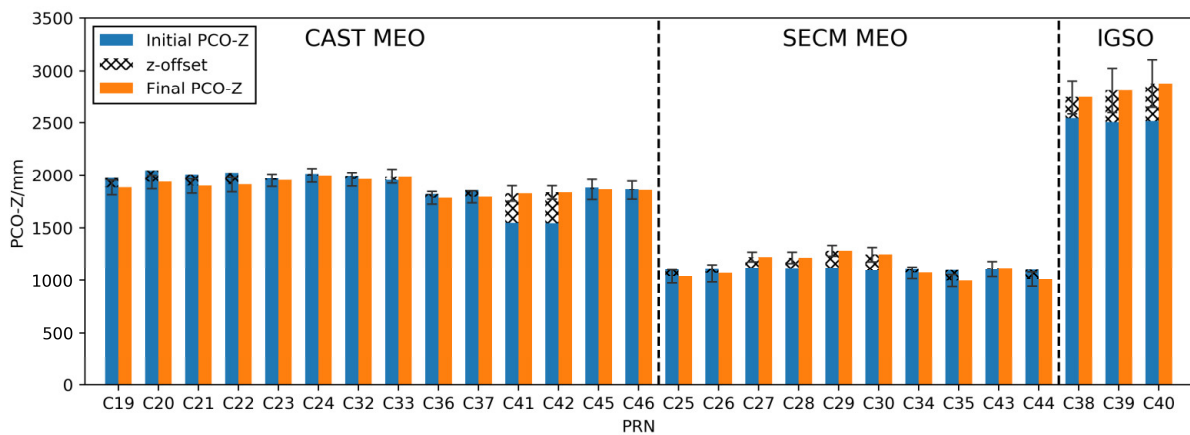


**Figure 6.** The initial PCO-Z, z-offsets, and the final PCO-Z. The z-offset is the correction of the initial PCO-Z, and the sum of the z-offset and initial PCO-Z is the final PCO-Z.

4.2. PCO-Z and PCVs

The PCVraw of the 3-Step Scheme is estimated with the PCO z-offset fix to Table 2, while the 2-Step Scheme fix to CSNO published values. Take C23, C29, C40, and C46 as examples, Figure 7 shows their daily PCVraw of the 2-Step Scheme, and the PCVraw of the 3-Step Scheme shows similar behavior. It can be seen that the consistency of daily PCVraw at the minimum and maximum nadir-angle are worse than the others, that is because only a few observations are available at these nadir-angles, and the weight of observations at the maximum nadir-angle is weak, the same phenomenon can also be seen from the other study of PCC model even with different signals such as B1I/B3I [15,17]. The consistency of daily PCVraw of C40 and C46 is worse than that of C23 and C29, mainly because of the above-mentioned SRP model deficiency. The final PCVraw models for each satellite are acquired by averaging the daily PCVraw after removing gross errors.

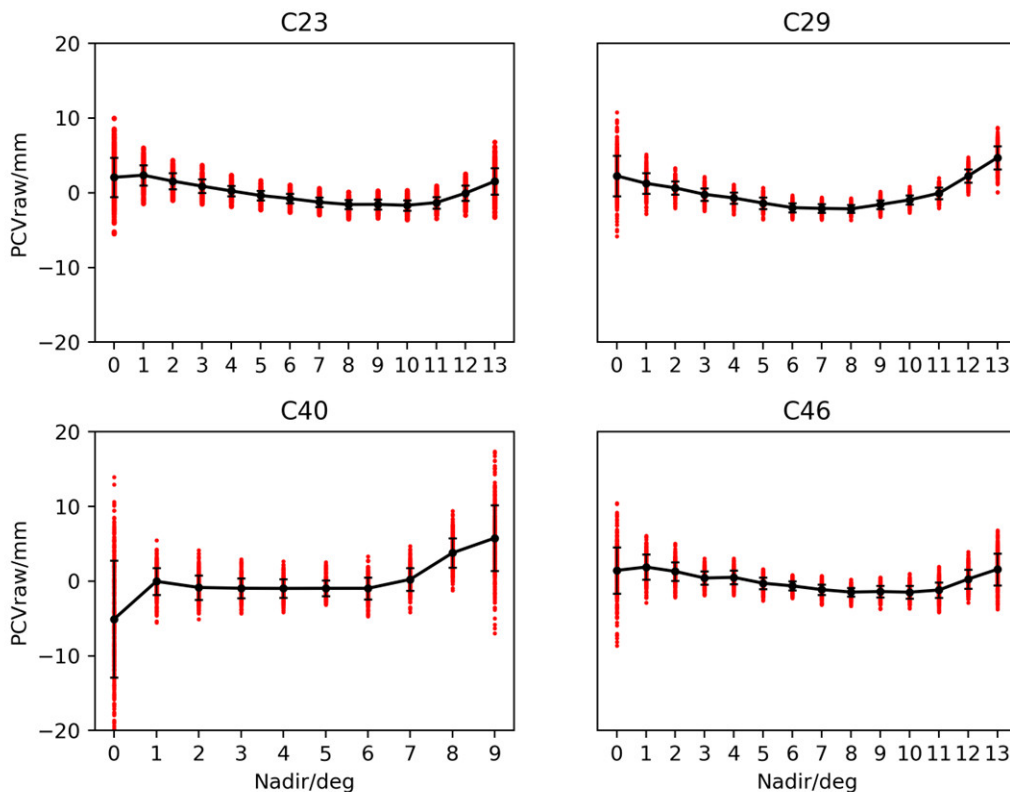
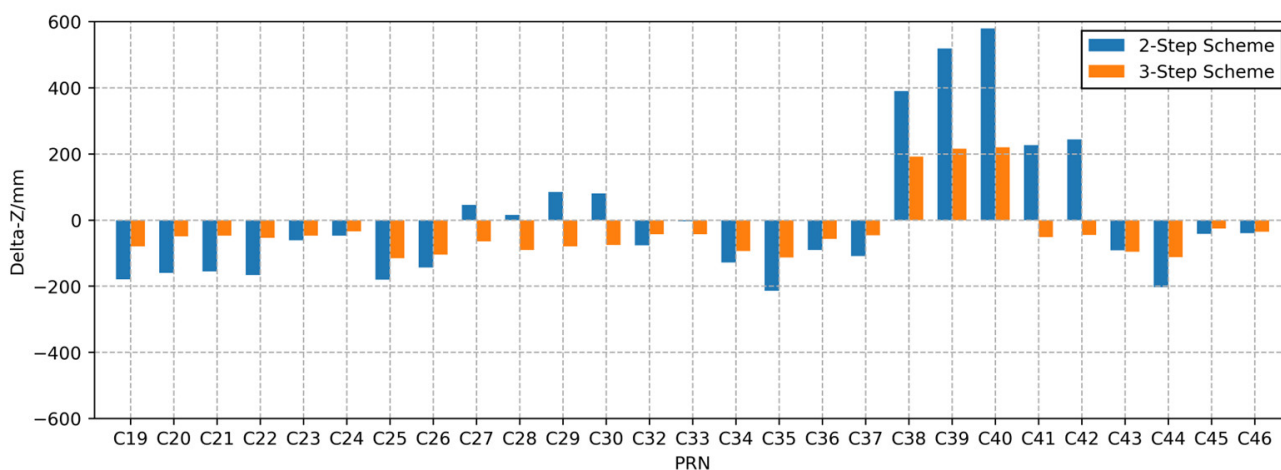


**Figure 7.** The daily PCVraw of C23, C29, C40, and C46, respectively.

The  $\Delta z$  derived from PCVraws of both schemes are listed in Table 3 with their final PCO z-offsets, and the difference between the two sets of PCO-Zs is also shown in the Diff column. It can be seen that the maximum PCO-Z difference is  $-2.24$  mm, which appears at C40. The absolute difference of MEO satellites does not exceed 1 mm, considering the RMSE of z-offset estimation is at the centimeter level, the difference can be ignored. The PCO-Zs of the two schemes agree well. Figure 8 provides a clear comparison of  $\Delta z$ , the majority of  $\Delta z$  absolute value of the 2-Step Scheme is large than that of the 3-Step Scheme, in the 2-Step Scheme, the omitted z-offset estimation in the PCO estimation process can be directly absorbed by PCVraw, and derived to  $\Delta z$ . That is to say, the 2-Step Scheme can handle the whole error that exists in the initial PCO z-offset as well as the 3-Step Scheme.

**Table 3.** The  $\Delta z$  and PCO-Z of both schemes, and the difference between the two sets of PCO-Zs, the unit is mm.

PRN	2-Step Scheme		3-Step Scheme		Diff	PRN	2-Step Scheme		3-Step Scheme		Diff
	$\Delta z$	PCO-Z	$\Delta z$	PCO-Z			$\Delta z$	PCO-Z	$\Delta z$	PCO-Z	
C19	-178.97	1800.75	-79.66	1800.82	-0.07	C34	-128.57	979.54	-93.91	979.26	0.28
C20	-159.39	1886.17	-49.16	1886.10	0.07	C35	-213.20	885.09	-112.95	884.87	0.22
C21	-155.52	1851.47	-46.73	1851.34	0.12	C36	-90.62	1726.10	-56.64	1726.17	-0.07
C22	-165.51	1856.54	-53.77	1856.41	0.13	C37	-109.08	1745.93	-46.06	1745.99	-0.06
C23	-61.33	1903.65	-46.52	1903.54	0.11	C38	390.38	2935.94	191.87	2936.64	-0.70
C24	-47.28	1965.21	-34.13	1965.28	-0.07	C39	519.39	3024.76	215.76	3025.88	-1.12
C25	-180.54	923.38	-115.65	923.26	0.12	C40	579.56	3095.85	220.47	3098.09	-2.24
C26	-143.29	964.50	-104	964.55	-0.05	C41	227.09	1772.39	-51.39	1771.81	0.57
C27	46.52	1161.95	-63.79	1162.18	-0.23	C42	243.85	1788.42	-45.07	1787.74	0.69
C28	15.47	1128.03	-89.76	1128.46	-0.43	C43	-90.94	1014.51	-95.99	1014.46	0.05
C29	84.61	1204.42	-79.67	1204.40	0.01	C44	-202.65	899.33	-111.92	899.40	-0.07
C30	80.39	1174.52	-74.71	1174.37	0.15	C45	-41.74	1837.29	-25.66	1837.03	0.25
C32	-76.23	1918.25	-43.06	1918.14	0.10	C46	-39.59	1822.04	-34.54	1822.00	0.04
C33	-3.38	1946.41	-42.91	1946.38	0.03						



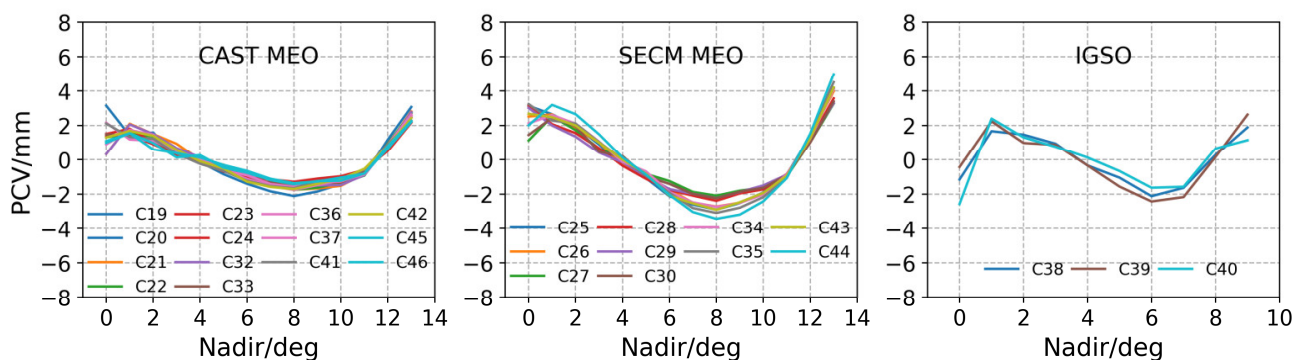
**Figure 8.** The  $\Delta z$  of 2-Step Scheme and 3-Step Scheme.

Table 4 is the PCV of the 3-Step Scheme, and Table 5 is the PCV of the 2-Step Scheme. The two sets of PCVs have nearly no difference. The maximum absolute difference is 0.12 mm and only appears at the  $0^\circ$  nadir-angle of C42, the other absolute difference does not exceed 0.03 mm, and the mean absolute difference is 0.004 mm, these differences can be safely ignored, which means the PCVs of the two schemes agree well too. The solution of the 2-Step Scheme is selected as the final PCC model of this study (Tables 3 and 5), Figure 9 shows the satellite-specific PCV of the 2-Step Scheme, and the satellites are grouped by block

type. The PCVs of the same block type show a similar pattern, but the in-type difference of PCV can reach several millimeters at a certain nadir-angle, therefore, satellite-specific PCVs are recommended [24].

**Table 4.** Final PCVs for each satellite of the 3-Step Scheme, the unit is mm.

PRN	Nadir-Angle/°													
	0°	1°	2°	3°	4°	5°	6°	7°	8°	9°	10°	11°	12°	13°
C19	3.12	1.44	1.23	0.43	-0.13	-0.84	-1.39	-1.83	-2.11	-1.84	-1.41	-0.91	1.18	3.07
C20	1.39	1.47	1.59	0.15	0.18	-0.52	-0.95	-1.43	-1.7	-1.44	-1.38	-0.84	0.75	2.75
C21	0.33	2.10	1.50	0.94	0.00	-0.3	-0.98	-1.53	-1.74	-1.67	-1.51	-0.82	0.86	2.81
C22	1.32	1.53	1.38	0.64	0.02	-0.41	-1.05	-1.47	-1.75	-1.62	-1.35	-0.92	0.97	2.72
C23	1.52	1.82	1.04	0.42	-0.16	-0.69	-0.99	-1.35	-1.52	-1.35	-1.30	-0.74	0.74	2.56
C24	1.45	1.43	0.91	0.30	-0.17	-0.52	-1.01	-1.14	-1.28	-1.10	-0.96	-0.59	0.52	2.16
C25	3.14	2.65	1.97	0.90	-0.23	-1.07	-2.12	-2.61	-2.89	-2.51	-1.90	-0.87	1.39	4.15
C26	2.52	2.64	1.87	1.02	-0.30	-0.85	-1.74	-2.49	-2.71	-2.49	-1.93	-0.91	1.38	3.98
C27	1.11	2.54	1.74	0.66	0.05	-0.82	-1.24	-1.87	-2.08	-1.79	-1.61	-0.98	1.03	3.27
C28	3.13	2.08	1.57	0.68	-0.35	-1.11	-1.75	-2.08	-2.38	-1.95	-1.72	-0.84	1.15	3.57
C29	3.01	2.00	1.35	0.42	-0.15	-0.95	-1.70	-1.98	-2.22	-1.87	-1.49	-0.87	1.16	3.29
C30	1.45	2.45	1.96	0.47	0.21	-0.96	-1.40	-1.98	-2.23	-1.85	-1.63	-0.90	1.02	3.39
C32	0.33	2.06	1.52	0.68	0.13	-0.44	-0.88	-1.43	-1.68	-1.48	-1.47	-0.89	0.76	2.78
C33	1.49	1.42	1.12	0.55	-0.09	-0.55	-1.14	-1.31	-1.48	-1.27	-1.16	-0.66	0.61	2.47
C34	2.13	2.61	2.11	1.08	-0.12	-0.69	-1.87	-2.47	-2.74	-2.51	-2.02	-0.86	1.24	4.11
C35	3.24	2.29	2.12	1.04	0.03	-0.92	-1.92	-2.80	-3.09	-2.78	-2.17	-1.07	1.50	4.52
C36	2.16	1.19	1.12	0.50	0.05	-0.65	-1.12	-1.53	-1.75	-1.46	-1.20	-0.87	0.92	2.63
C37	0.90	1.75	1.46	0.40	0.12	-0.64	-0.9	-1.41	-1.57	-1.34	-1.26	-0.81	0.76	2.54
C38	-1.14	1.67	1.47	0.95	-0.34	-1.05	-2.11	-1.63	0.29	1.89				
C39	-0.42	2.25	0.99	0.88	-0.34	-1.56	-2.42	-2.16	0.15	2.64				
C40	-2.56	2.40	1.33	0.77	0.12	-0.65	-1.63	-1.58	0.65	1.17				
C41	2.15	1.33	1.23	0.34	-0.25	-0.66	-1.23	-1.54	-1.66	-1.23	-1.13	-0.58	0.93	2.29
C42	1.43	1.66	1.40	0.55	-0.12	-0.52	-1.28	-1.59	-1.71	-1.41	-1.12	-0.53	0.80	2.44
C43	2.66	2.50	2.01	1.01	0.00	-0.82	-2.09	-2.52	-2.90	-2.46	-1.92	-0.93	1.26	4.20
C44	2.01	3.19	2.66	1.50	0.14	-0.87	-2.04	-3.03	-3.42	-3.18	-2.41	-1.07	1.53	4.99
C45	0.99	1.57	0.61	0.38	0.12	-0.31	-0.65	-1.11	-1.36	-1.26	-1.04	-0.81	0.66	2.21
C46	1.10	1.56	0.98	0.13	0.27	-0.47	-0.76	-1.18	-1.42	-1.25	-1.22	-0.81	0.80	2.26



**Figure 9.** Satellite-specific PCV of the 2-Step Scheme.

**Table 5.** Final PCVs for each satellite of the 2-Step Scheme, the unit is mm.

PRN	Nadir-Angle/°													
	0°	1°	2°	3°	4°	5°	6°	7°	8°	9°	10°	11°	12°	13°
C19	3.15	1.42	1.22	0.42	−0.14	−0.84	−1.40	−1.83	−2.11	−1.84	−1.41	−0.91	1.19	3.07
C20	1.38	1.47	1.60	0.15	0.17	−0.52	−0.95	−1.43	−1.70	−1.45	−1.38	−0.83	0.75	2.74
C21	0.33	2.10	1.50	0.94	0.00	−0.30	−0.98	−1.53	−1.74	−1.67	−1.51	−0.82	0.86	2.82
C22	1.31	1.53	1.38	0.64	0.02	−0.40	−1.05	−1.47	−1.75	−1.62	−1.35	−0.92	0.97	2.71
C23	1.52	1.81	1.04	0.42	−0.16	−0.69	−0.99	−1.35	−1.52	−1.35	−1.30	−0.74	0.74	2.56
C24	1.44	1.44	0.91	0.30	−0.17	−0.52	−1.01	−1.14	−1.28	−1.10	−0.96	−0.59	0.52	2.16
C25	3.14	2.65	1.97	0.90	−0.24	−1.07	−2.11	−2.60	−2.89	−2.51	−1.90	−0.87	1.39	4.15
C26	2.52	2.64	1.87	1.02	−0.29	−0.85	−1.74	−2.49	−2.71	−2.49	−1.93	−0.91	1.38	3.98
C27	1.13	2.52	1.74	0.66	0.05	−0.82	−1.24	−1.87	−2.08	−1.79	−1.62	−0.98	1.03	3.27
C28	3.14	2.08	1.56	0.68	−0.35	−1.11	−1.75	−2.08	−2.38	−1.95	−1.72	−0.84	1.15	3.57
C29	3.01	2.00	1.35	0.42	−0.15	−0.95	−1.70	−1.97	−2.22	−1.87	−1.49	−0.87	1.16	3.29
C30	1.45	2.45	1.96	0.47	0.21	−0.96	−1.40	−1.98	−2.23	−1.85	−1.63	−0.90	1.02	3.39
C32	0.33	2.06	1.51	0.68	0.13	−0.44	−0.88	−1.43	−1.67	−1.49	−1.47	−0.89	0.77	2.78
C33	1.49	1.42	1.12	0.55	−0.09	−0.55	−1.14	−1.30	−1.48	−1.27	−1.16	−0.66	0.61	2.46
C34	2.13	2.60	2.11	1.07	−0.13	−0.68	−1.87	−2.47	−2.73	−2.50	−2.02	−0.86	1.24	4.10
C35	3.24	2.28	2.12	1.05	0.03	−0.92	−1.92	−2.80	−3.08	−2.78	−2.17	−1.06	1.50	4.51
C36	2.16	1.19	1.12	0.50	0.05	−0.65	−1.11	−1.52	−1.75	−1.47	−1.20	−0.87	0.92	2.63
C37	0.90	1.75	1.46	0.41	0.12	−0.64	−0.91	−1.41	−1.57	−1.34	−1.26	−0.81	0.76	2.54
C38	−1.15	1.67	1.47	0.95	−0.34	−1.04	−2.11	−1.63	0.29	1.89				
C39	−0.42	2.24	0.99	0.88	−0.34	−1.56	−2.42	−2.17	0.16	2.63				
C40	−2.56	2.40	1.31	0.76	0.13	−0.66	−1.62	−1.57	0.66	1.15				
C41	2.12	1.34	1.24	0.35	−0.24	−0.66	−1.22	−1.54	−1.65	−1.23	−1.13	−0.58	0.92	2.29
C42	1.31	1.69	1.41	0.58	−0.09	−0.51	−1.28	−1.58	−1.70	−1.41	−1.12	−0.53	0.79	2.43
C43	2.68	2.48	2.00	1.01	0.00	−0.82	−2.08	−2.53	−2.90	−2.46	−1.92	−0.93	1.26	4.20
C44	2.02	3.20	2.66	1.49	0.14	−0.87	−2.04	−3.03	−3.42	−3.18	−2.41	−1.07	1.53	4.99
C45	1.00	1.56	0.61	0.38	0.12	−0.31	−0.65	−1.11	−1.36	−1.27	−1.04	−0.81	0.66	2.21
C46	1.09	1.55	0.98	0.13	0.27	−0.46	−0.76	−1.18	−1.42	−1.25	−1.22	−0.80	0.80	2.26

## 5. Validations

The estimated vertical PCO and PCV are verified by examining the qualities of the BDS-3 orbits and BDS-only PPP solutions, they are performed with the estimated PCC model (named PCC Scheme), and the same products produced with the CSNO-released PCC model (named CSNO Scheme) used as a comparison. The POD strategy is the same as in Table 1, except no PCO or PCVraw is estimated, and the stations are the same as in Figure 2. We use the 3-dimension RMS (3D RMS) of Orbit Day boundary discontinuity (DBD) [39] to evaluate the orbit quality. Figure 10 shows the mean 3D RMS of each satellite for both CSNO and PCC Schemes. The orbit qualities of MEO satellites are significantly better than that of IGSO satellites, and the orbit qualities of the two schemes show no clear differences, that is because the difference of the PCC model can be absorbed by the other parameters like clock offset in the POD process. Table 6 summarizes the block-type mean differences of the orbit qualities of the two schemes, compared with the CSNO Scheme, the orbit quality of the PCC Scheme improved by 4.8%, 7.0%, and −0.8% for CAST MEO, SECM MEO, and IGSO satellites, respectively.

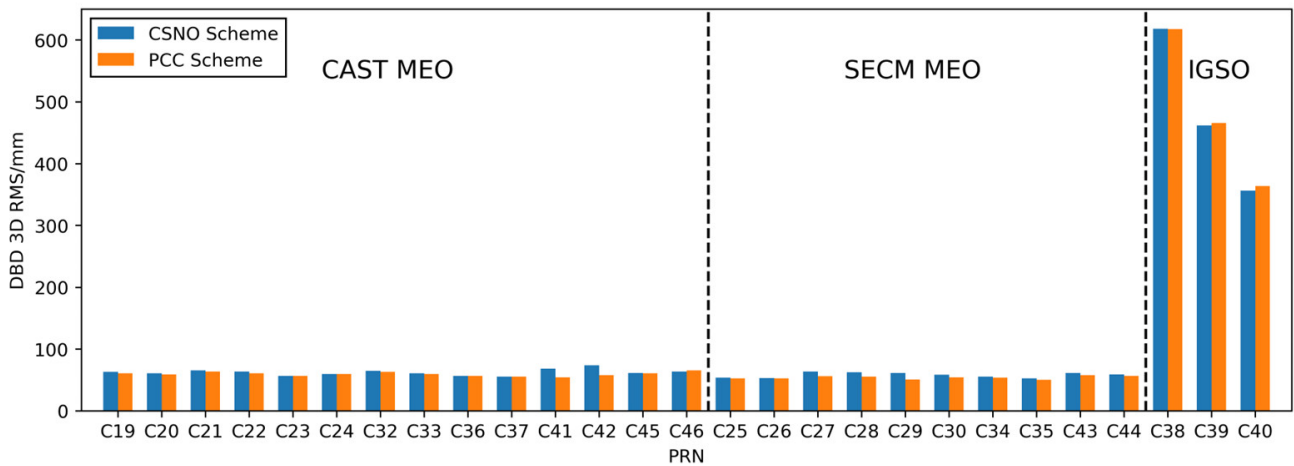


Figure 10. The mean orbit DBD 3D RMS of CSNO and PCC Schemes.

Table 6. Orbit DBD 3D RMS difference of each scheme and their comparison, the unit is mm.

Scheme	CAST MEO	SECM MEO	IGSO
CSNO	62.7	58.3	478.9
PCC	59.7	54.2	482.6
Improvement (%)	4.8%	7.0%	−0.8%

Since the orbit qualities of IGSO satellites behave abnormally, their DBD in along-track (A), cross-track (C), radial (R), and 3D RMS time series of the CSNO Scheme have been analyzed in Figure 11. We also compared the IGSO satellites’ orbits with the Wuhan University IGS AC (WUM) rapid orbit products, and the results are shown in Figure 12. It is obvious that the DBD has a periodic term related to the  $\beta$  angle in any direction, the periodic term in the radial direction is the most obvious for C39 with the largest  $\beta$  angle range, and the periodic term has the largest peak. The periodic term may cause by the SRP model deficiency mentioned in Section 4.1, the results of orbit differences with WUM products also have the periodic term, but with a much smaller magnitude, the POD strategies and SRP model used by WUM may be similar to the CSNO Scheme, hence, their orbits have a good consistency, and the DBD may be more sensitive to the model deficiency. Due to the SRP model deficiency, the IGSO satellites PCC model estimated in this study is not accurate and needs further study together with the SRP model.

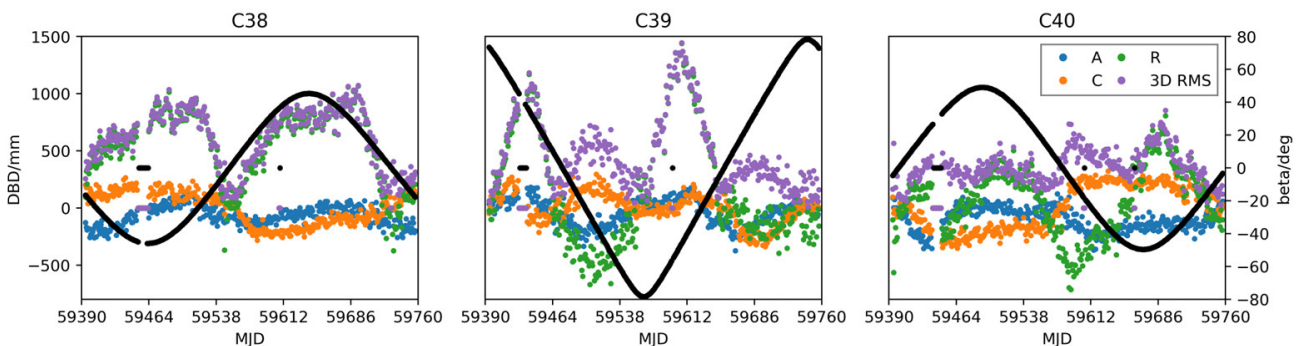
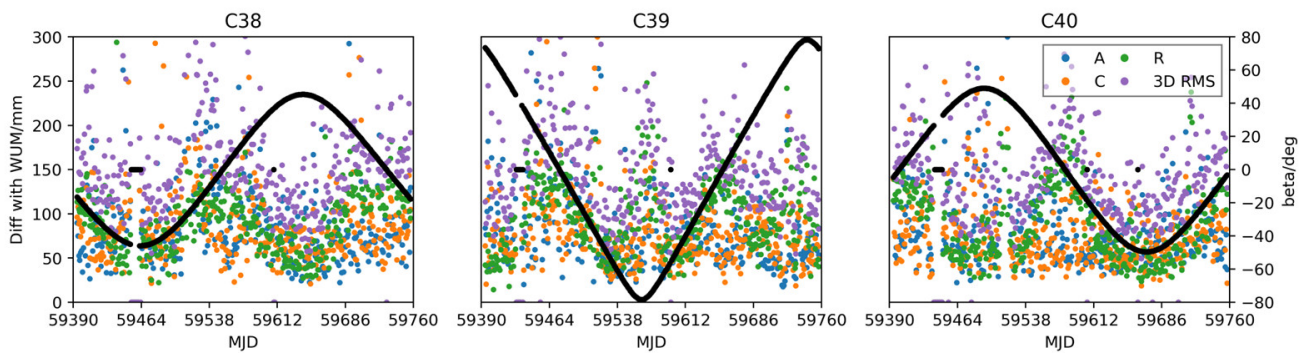
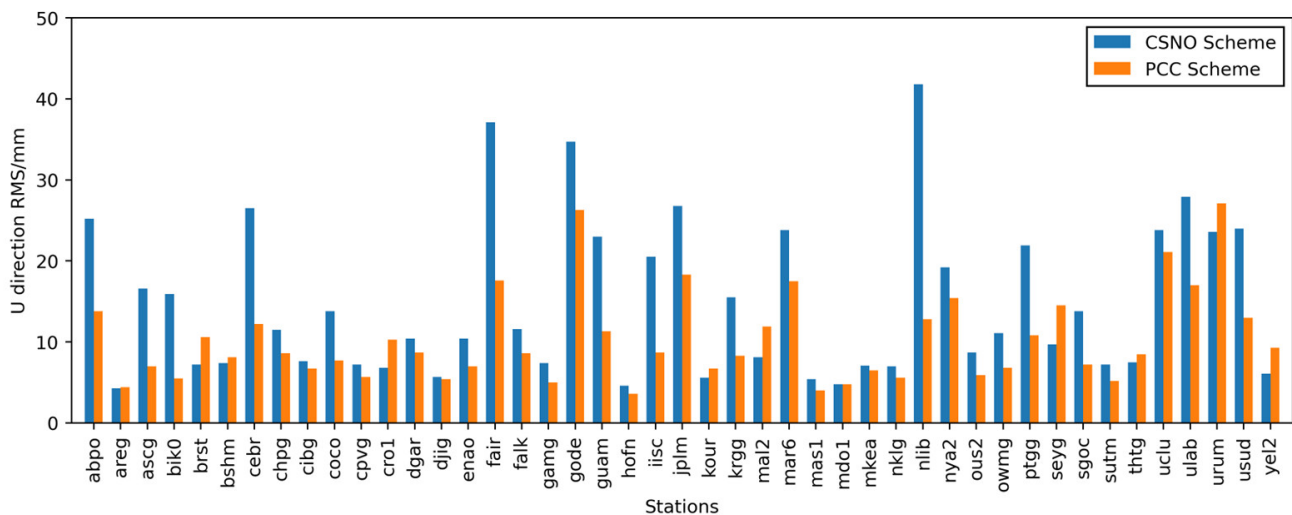


Figure 11. The IGSO orbit DBD time series of the CSNO Scheme in the along-track (A), cross-track (C), radial (R), and 3D RMS.



**Figure 12.** The time series of the differences of the CSNO Scheme IGSO orbit compared with the WUM products in along-track (A), cross-track (C), radial (R), and 3D RMS.

It is well known that the vertical PCO and PCV have a significant influence on the PPP solutions, especially in the up direction (U) [24]. We carry out a BDS-only PPP comparison to further study the quality of the proposed vertical PCO and PCV, 45 MGEX stations, which can track the B1C/B2a signals selected and marked as blue triangles in Figure 2. The orbit and clock products generated by the corresponding POD scheme are used for the PPP process, and 30 days of data from DOY 120, 2022, to DOY 149, 2022, is processed. The IGS weekly solution is selected as a reference. Figure 13 demonstrates the U-direction RMS of each station, for most stations, the PCC Scheme solutions have a clear advantage. The mean RMS of the north (N), east (E), and U directions are listed in Table 7, compared with the CSNO scheme, the accuracy of the PCC Scheme improved by 30.0%, 27.2%, and 31.1% for N, E, and U directions, respectively.



**Figure 13.** The station U-direction RMS for BDS-only PPP solutions of CSNO and PCC Schemes.

**Table 7.** BDS-only PPP RMS of each scheme and their comparison, the unit is mm.

Scheme	N	E	U
CSNO	5	8.1	14.8
PCC	3.5	5.9	10.2
Improvement (%)	30.0%	27.2%	31.1%

## 6. Summary and Discussions

The BDS-3 started to transmit the newly designed B1C/B2a signals to global users, however, the PCC models of B1C/B2a signals have not been thoroughly studied. In this study, we focus on the vertical component of the PCO and PCV model, one-year data have been processed to estimate the vertical PCO and PCV. Two PCC model estimation schemes have been introduced and discussed. The proposed PCC model of the B1C/B2a signals is verified by the POD and BDS-only PPP qualities by comparing with the CSNO-released PCC model.

The PCO and PCV usually be estimated separately because of the strong correlation between PCO z-offset and the PCV. Both PCO and PCV estimations are performed by the POD process and estimated together with the orbital parameters, therefore, the traditional PCC model estimation is quite time-consuming. The PCO estimation provides a precise z-offset for the subsequent process, with a coarse z-offset value, proper constraint, and adjustment method, the PCO estimation can be omitted. The newly proposed 2-Step Scheme is compared with the traditional 3-Step Scheme, and the estimated parameters have been analyzed.

The z-offset is only estimated by the 3-Step Scheme. The z-offset series are quite stable except for the z-offset of the IGSO satellites and the MEO satellites with Pseudo Random Noise code (PRN) C45 and C46. The IGSO satellite is equipped with communication antennas, which are not considered in the SRP model; the satellite structure of C45 and C46 are also different from the other MEO satellites [18], and these differences cause the SRP model deficiency. The period terms related to the  $\beta$  angle exist in the z-offset series of IGSO satellites and C45/C46 may be caused by the SRP model deficiency.

The comparison of  $\Delta z$  separated from the PCVraws of the two schemes confirmed that the PCVraw can comprehensively absorb the error of the initial PCO z-offset and derive it to the  $\Delta z$ . The final PCO z-offset and PCV derived from the two schemes consist very well, with mean absolute differences do not exceed 1 mm and 0.01 mm for PCO z-offset and PCV, respectively. This result proved the validity of the proposed 2-Step Scheme. We select the solution of the 2-Step Scheme as the final PCC model of this study (Tables 3 and 5).

The proposed PCC model is compared with the CSNO-released PCC model to verify its quality. The mean 3D RMS of orbit DBD for MEO satellites shows a little improvement, while the orbit qualities of the IGSO satellites have a slight decrease. The orbit DBDs of IGSO satellites are significantly worse than that of MEO satellites and have a clear periodic term related to the  $\beta$  angle, which was also caused by the SRP model deficiency. The comparisons between IGSO orbits and WUM AC orbit products confirmed the periodic term and indicated that no other apparent model errors were found in the orbit determination of IGSO satellites. The BDS-only PPP solution of the PCC Scheme shows a clear improvement compared to that of the CSNO Scheme, which denotes that the proposed PCC model of the B1C/B2a signals is accurate.

It is worth noticing that only the vertical PCO component is considered in this study, since the horizontal PCO components have strong correlations with SRP parameters, and the SRP model of BDS-3 satellites is not very accurate, especially for the IGSO satellites and C45/C46. Further study should be carried out to build a rigorous SRP model for the BDS-3 satellites. And the receiver antenna PCC models of BDS signals for the IGB 14 framework are still missing, luckily, the IGS ATX files for the IGB R3 and upcoming IGB 20 frameworks provide some receiver antenna PCC models for BDS signals. With the related model being improved, the BDS PCC model can be estimated more accurately in orbit.

**Author Contributions:** Conceptualization, S.X. and G.H.; methodology, S.X., L.W. and X.Y.; validation, L.W. and Z.Q.; formal analysis, S.X., G.H. and X.Y.; writing—original draft preparation, S.X.; writing—review and editing, S.X., G.H., L.W., X.Y. and Z.Q.; funding acquisition, G.H. All authors have read and agreed to the published version of the manuscript.

**Funding:** This work was supported by the Key R&D Program of Shaanxi Province (2022ZDLSF07-12), the Special Fund for Basic Scientific Research of Central Colleges (Grant No. CHD300102269305, CHD300102268305, Chang'an University).

**Data Availability Statement:** The observations analyzed during the current study are available from: <ftp://igs.gnsswhu.cn/pub/gps/> (accessed on 7 November 2022). The CSNO antenna file is available from: <http://en.beidou.gov.cn/SYSTEMS/Officialdocument/201912/P020200103555670269778.atx> (accessed on 7 November 2022). The IGS antenna files are available from: [http://ftp.aiub.unibe.ch/users/villiger/igsR3\\_2077.atx](http://ftp.aiub.unibe.ch/users/villiger/igsR3_2077.atx) (accessed on 7 November 2022) and [ftp://igs.ign.fr/pub/igs/igs\\_cb/station/general/](ftp://igs.ign.fr/pub/igs/igs_cb/station/general/) (accessed on 7 November 2022). The satellite information of BDS is available from: <http://en.beidou.gov.cn/SYSTEMS/Officialdocument/201912/P020200103556125703019.rar> (accessed on 7 November 2022).

**Acknowledgments:** The authors would like to thank the anonymous reviewers and the editors for their constructive comments of this manuscript. The authors would also thank for the data support of the CSNO and the IGS.

**Conflicts of Interest:** The authors declare no conflict of interest.

## References

1. Yang, Y.; Liu, L.; Li, J.; Yang, Y.; Zhang, T.; Mao, Y.; Sun, B.; Ren, X. Featured services and performance of BDS-3. *Sci. Bull.* **2021**, *66*, 2135–2143. [CrossRef]
2. Ye, F.; Yuan, Y.; Yang, Z. Validation and evaluation on B1IB3I-based and B1CB2a-based BDS-3 precise orbits from iGMAS. *Adv. Space Res.* **2022**, *70*, 2167–2177. [CrossRef]
3. Yang, Y.; Gao, W.; Guo, S.; Mao, Y.; Yang, Y. Introduction to BeiDou-3 navigation satellite system. *Navigation* **2019**, *66*, 7–18. [CrossRef]
4. Lu, J.; Guo, X.; Su, C. Global capabilities of BeiDou Navigation Satellite System. *Satell. Navig.* **2020**, *1*, 16. [CrossRef]
5. Li, R.; Wang, N.; Li, Z.; Zhang, Y.; Wang, Z.; Ma, H. Precise orbit determination of BDS-3 satellites using B1C and B2a dual-frequency measurements. *GPS Solut.* **2021**, *25*, 95. [CrossRef]
6. Schmid, R.; Steigenberger, P.; Gendt, G.; Ge, M.; Rothacher, M. Generation of a consistent absolute phase-center correction model for GPS receiver and satellite antennas. *J. Geod.* **2007**, *81*, 781–798. [CrossRef]
7. Zhang, X.; Wu, M.; Liu, W.; Li, X.; Yu, S.; Lu, C.; Wickert, J. Initial assessment of the COMPASS/BeiDou-3: New-generation navigation signals. *J. Geod.* **2017**, *91*, 1225–1240. [CrossRef]
8. Yan, X.; Huang, G.; Zhang, Q.; Liu, C.; Wang, L.; Qin, Z. Early analysis of precise orbit and clock offset determination for the satellites of the global BeiDou-3 system. *Adv. Space Res.* **2019**, *63*, 1270–1279. [CrossRef]
9. Zhang, Y.; Kubo, N.; Chen, J.; Wang, J.; Wang, H. Initial Positioning Assessment of BDS New Satellites and New Signals. *Remote Sens.* **2019**, *11*, 1320. [CrossRef]
10. Schmid, R.; Dach, R.; Collilieux, X.; Jäggi, A.; Schmitz, M.; Dilssner, F. Absolute IGS antenna phase center model igs08.atx: Status and potential improvements. *J. Geod.* **2015**, *90*, 343–364. [CrossRef]
11. BeiDou Navigation Satellite System. Satellite Antenna Phase Center of BDS. Available online: <http://en.beidou.gov.cn/SYSTEMS/Officialdocument/201912/P020200103555670269778.atx> (accessed on 7 November 2022).
12. Dilssner, F.; Springer, T.; Schönemann, E.; Enderle, W. Estimation of satellite antenna phase center corrections for BeiDou. In Proceedings of the IGS Workshop, Pasadena, CA, USA, 23–27 June 2014; pp. 23–27.
13. Guo, J.; Xu, X.; Zhao, Q.; Liu, J. Precise orbit determination for quad-constellation satellites at Wuhan University: Strategy, result validation, and comparison. *J. Geod.* **2015**, *90*, 143–159. [CrossRef]
14. Huang, G.; Yan, X.; Zhang, Q.; Liu, C.; Wang, L.; Qin, Z. Estimation of antenna phase center offset for BDS IGSO and MEO satellites. *GPS Solut.* **2018**, *22*, 49. [CrossRef]
15. Yan, X.; Huang, G.; Zhang, Q.; Wang, L.; Qin, Z.; Xie, S. Estimation of the Antenna Phase Center Correction Model for the BeiDou-3 MEO Satellites. *Remote Sens.* **2019**, *11*, 2850. [CrossRef]
16. Xia, F.; Ye, S.; Chen, D.; Wu, J.; Wang, C.; Sun, W. Estimation of antenna phase center offsets for BeiDou IGSO and MEO satellites. *GPS Solut.* **2020**, *24*, 90. [CrossRef]
17. Qu, Z.; Guo, J.; Zhao, Q. Phase Center Corrections for BDS IGSO and MEO Satellites in IGB14 and IGSR3 Frame. *Remote Sens.* **2021**, *13*, 745. [CrossRef]
18. Zajdel, R.; Steigenberger, P.; Montenbruck, O. On the potential contribution of BeiDou-3 to the realization of the terrestrial reference frame scale. *GPS Solut.* **2022**, *26*, 109. [CrossRef]
19. Montenbruck, O.; Schmid, R.; Mercier, F.; Steigenberger, P.; Noll, C.; Fatkulin, R.; Kogure, S.; Ganeshan, A.S. GNSS satellite geometry and attitude models. *Adv. Space Res.* **2015**, *56*, 1015–1029. [CrossRef]
20. Steigenberger, P.; Fritsche, M.; Dach, R.; Schmid, R.; Montenbruck, O.; Uhlemann, M.; Prange, L. Estimation of satellite antenna phase center offsets for Galileo. *J. Geod.* **2016**, *90*, 773–785. [CrossRef]

21. Zhu, S.Y.; Massmann, F.H.; Yu, Y.; Reigber, C. Satellite antenna phase center offsets and scale errors in GPS solutions. *J. Geod.* **2003**, *76*, 668–672. [[CrossRef](#)]
22. Ge, M. Impact of GPS satellite antenna offsets on scale changes in global network solutions. *Geophys. Res. Lett.* **2005**, *32*, L06310. [[CrossRef](#)]
23. Schmid, R.; Rothacher, M. Estimation of elevation-dependent satellite antenna phase center variations of GPS satellites. *J. Geod.* **2003**, *77*, 440–446. [[CrossRef](#)]
24. Xie, S.; Huang, G.; Wang, L.; Yan, X.; Qin, Z.; Cao, Y. A Refinement of Antenna Phase Center Correction Model for BDS IGSO and MEO Satellites. *J. Geod.* **2022**; *submitted*.
25. Chen, J.; Wang, J.; Yu, C.; Zhang, Y.; Wang, B. Improving BDS broadcast ephemeris accuracy using ground-satellite-link observations. *Satell. Navig.* **2022**, *3*, 11. [[CrossRef](#)]
26. Montenbruck, O.; Steigenberger, P.; Hugentobler, U. Enhanced solar radiation pressure modeling for Galileo satellites. *J. Geod.* **2014**, *89*, 283–297. [[CrossRef](#)]
27. Beutler, G.; Brockmann, E.; Gurtner, W.; Hugentobler, U.; Mervart, L.; Rothacher, M.; Verdun, A. Extended orbit modeling techniques at the CODE processing center of the international GPS service for geodynamics (IGS): Theory and initial results. *manuscripta geodaetica*. **1994**, *19*, 367–386.
28. Springer, T.A.; Beutler, G.; Rothacher, M. A New Solar Radiation Pressure Model for GPS Satellites. *GPS Solut.* **1999**, *2*, 50–62. [[CrossRef](#)]
29. Arnold, D.; Meindl, M.; Beutler, G.; Dach, R.; Schaer, S.; Lutz, S.; Prange, L.; Sošnica, K.; Mervart, L.; Jäggi, A. CODE's new solar radiation pressure model for GNSS orbit determination. *J. Geod.* **2015**, *89*, 775–791. [[CrossRef](#)]
30. Li, X.; Yuan, Y.; Zhu, Y.; Jiao, W.; Bian, L.; Li, X.; Zhang, K. Improving BDS-3 precise orbit determination for medium earth orbit satellites. *GPS Solut.* **2020**, *24*, 53. [[CrossRef](#)]
31. BeiDou Navigation Satellite System. Satellite Information of BDS. Available online: <http://en.beidou.gov.cn/SYSTEMS/Officialdocument/201912/P020200103556125703019.rar> (accessed on 7 November 2022).
32. Zhao, Q.; Guo, J.; Wang, C.; Lyu, Y.; Xu, X.; Yang, C.; Li, J. Precise orbit determination for BDS satellites. *Satell. Navig.* **2022**, *3*, 2. [[CrossRef](#)]
33. Solano, C.J.R. Impact of Albedo modelling in GPS orbits. 2009.
34. Steigenberger, P.; Thoenert, S.; Montenbruck, O. GNSS satellite transmit power and its impact on orbit determination. *J. Geod.* **2017**, *92*, 609–624. [[CrossRef](#)]
35. Steigenberger, P.T.S. Initial BDS-3 transmit power analysis (with BDS-2 gain pattern). 2020.
36. Saastamoinen, J. Contributions to the theory of atmospheric refraction. *Bull. Géodésique* **2008**, *105*, 279–298. [[CrossRef](#)]
37. Boehm, J.; Niell, A.; Tregoning, P.; Schuh, H. Global Mapping Function (GMF): A new empirical mapping function based on numerical weather model data. *Geophys. Res. Lett.* **2006**, *33*, L07304. [[CrossRef](#)]
38. Ge, M.; Gendt, G.; Dick, G.; Zhang, F.P. Improving carrier-phase ambiguity resolution in global GPS network solutions. *J. Geod.* **2005**, *79*, 103–110. [[CrossRef](#)]
39. Griffiths, J.; Ray, J.R. On the precision and accuracy of IGS orbits. *J. Geod.* **2009**, *83*, 277–287. [[CrossRef](#)]